Chemosphere 144 (2016) 1050–1059

Contents lists available at ScienceDirect

Chemosphere

journal homepage: www.elsevier.com/locate/chemosphere

Interactions of benzotriazole UV stabilizers with human serum albumin: Atomic insights revealed by biosensors, spectroscopies and molecular dynamics simulations

Shulin Zhuang [a, b, *], Haifei Wang [a, b], Keke Ding [a], Jiaying Wang [a], Liumeng Pan [a], Yanli Lu [c], Qingjun Liu [c], Chunlong Zhang [d]

[a] Institute of Environmental Science, College of Environmental and Resource Sciences, Zhejiang University, Hangzhou 310058, China
[b] Key Laboratory of Health Risk Factors for Seafood of Zhejiang Province, Zhoushan 316022, China
[c] Biosensor National Special Laboratory, Key Laboratory of Biomedical Engineering of Education Ministry, Department of Biomedical Engineering, Zhejiang University, Hangzhou 310027, China
[d] Department of Environmental Sciences, University of Houston-Clear Lake, 2700 Bay Area Blvd., Houston, TX 77058, USA

HIGHLIGHTS

- The interaction of BZTs with human serum albumin was deciphered for the first time.
- Fluorescence of human serum albumin was quenched in a concentration-dependent mode.
- BZTs bind at the Sudlow site I site with distinct binding modes.
- Minor changes in the moieties of BZTs may affect their interactions with HSA.
- Our *in vitro* and *in silico* approach is helpful to assess risk of BZTs chemicals.

GRAPHICAL ABSTRACT

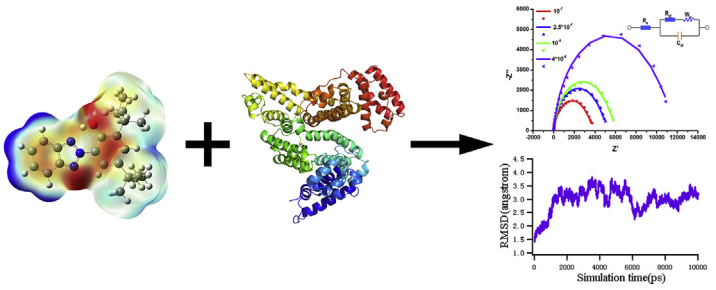

ARTICLE INFO

Article history:
Received 15 July 2015
Received in revised form
16 September 2015
Accepted 22 September 2015
Available online xxx

Keywords:
Benzotriazole
Biosensor
Spectroscopy
Molecular modeling
Human serum albumin

ABSTRACT

Benzotriazole UV stabilizers (BZTs) belong to one prominent group of ultraviolet (UV) stabilizers and are widely used in various plastics materials. Their large production volumes, frequent detections in the environment and potential toxicities have raised increasing public concern. BZTs can be transported *in vivo* by transport proteins in plasma and the binding association to transport proteins may serve as a significant parameter to evaluate the bioaccumulative potential. We utilized a novel HSA biosensor, circular dichroism spectroscopy, fluorescence spectroscopy to detect the dynamic interactions of six BZTs (UV-326, UV-327, UV-328, UV-329, UV-P, and BZT) with human serum albumin (HSA), and characterized the corresponding structure-activity relationships (SAR) by molecular dynamics simulations. All test BZTs potently bind at Sudlow site I of HSA with a binding constant of 10^4 L/mol at 298 K. Minor changes in the moieties of BZTs affect their interactions with HSA and differently induce conformations of HSA. Their binding reduced electrochemical impedance spectra and α-helix content of HSA, caused slight red-shifted emission, and changed fluorescence lifetime components of HSA in a concentration-dependent

* Corresponding author. College of Environmental and Resource Sciences, Zhejiang University, Hangzhou 310058, China.
E-mail address: shulin@zju.edu.cn (S. Zhuang).

http://dx.doi.org/10.1016/j.chemosphere.2015.09.085

mode. UV-327 and UV-329 form hydrogen bonds with HSA, while UV-329, UV-P and BZT bind HSA with more favorable electrostatic interactions. Our *in vitro* and *in silico* study offered a significant framework toward the understanding of risk assessment of BZTs and provides guide for future design of environmental benign BZTs-related materials.

1. Introduction

Benzotriazoles (BZTs) belong to a prominent group of ultraviolet (UV) stabilizers and have a structural feature of a benzotriazole moiety attached by a phenolic group (Table 1). BZTs can be polymerized or copolymerized with other chemicals. These anthropogenic chemicals have been used in personal hygiene products, sports equipment, industry and building materials, automobile components and circulating water treatment agents to prevent from UV-induced yellowing and degradation. Due to their high production volume and wide application, BZTs have been frequently detected in various environmental matrices such as municipal wastewater, sewage sludge, sediment, soil, and indoor dust (Ruan et al., 2012; Zhang et al., 2011; Song et al., 2014). BZTs were reportedly persistent and thus can be bioaccumulated and biomagnified in marine organisms and wildlife through food chain or trophic transfer in both aquatic and terrestrial systems (Nakata et al., 2010, 2009).

The widespread contamination of BZTs indicates a potential exposure and raises a serious public health concern. BZTs at environmentally relevant concentrations were reported to have the estrogenic potential in marine medaka (He et al., 2012). UV-P, UV-9, UV-326 and UV-090 were reported to have potent human ligand activity toward aryl hydrocarbon receptor (AhR) (Nagayoshi et al., 2015). UV-P caused dermatitis and skin irritation and UV-327 induced the gender-related difference in the toxicity toward young rats (Hirata-Koizumi et al., 2008). UV-328 and UV-320 have repeated-dose toxicity effects to rats. The increasing toxicological studies on BZTs prompt the need for an insightful examination over the molecular-level events between BZTs and biomacromolecules, however, as yet few relevant studies have been carried out.

The persistent and bioacculmulative properties render BZTs to be readily absorbed through skin and accumulated in blood, potentially causing interactions with plasma proteins. The transportation, distribution and metabolic processes of many exogenous ligands are highly dependent on their binding with human serum albumin (HSA), the most abundant transport protein in human plasma (Chi and Liu, 2011; Ghuman et al., 2005). HSA primarily acts as the carrier protein for the transportation of various exogenous and endogenous molecules (Yasar et al., 2011; Zhang et al., 2013a, b; Beauchemin et al., 2007; Hu et al., 2010; Xie et al., 2011). The extracellular HSA was reported to be a critical regulator of intercellular fluxes and can have interactions with other proteins such as CYP450 enzymes (Kandel and Lampe, 2014). The binding of HSA was suggested to be an important determinant for MPO (human neutrophil enzyme myeloperoxidase)-mediated SWCNT (carboxylated single-walled carbon nanotubes) biodegradation in human inflammatory cells (He and Carter, 1992). The binding of BZTs may have an adverse effect on the conformation and biological function of HSA, possibly resulting in the biological disorders. HSA has three structurally similar helical domains (I, II, and III), each composed of A and B subdomains (Ghuman et al., 2005; He and Carter, 1992). HSA generally has two binding cavities at subdomain IIA and IIIA (also called as Sudlow site I and Sudlow site II, respectively). The association constant of ligands to serum protein may be a useful parameter to characterize their bioaccumulative potential and *in vivo* bioavailability (Bischel et al., 2010), therefore, the dynamic interactions of BZTs with HSA need to be fully elucidated, which is of significance to facilitate the evaluation of their bioaccumulative potential. However, to date no such studies have been carried out at the atomic level.

Table 1
The structures of five BZTs.

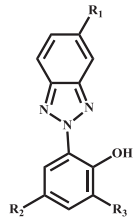

BZTs	R_1	R_2	R_3
UV-P	–	CH_3	–
UV-326	Cl	CH_3	$C(CH_3)_3$
UV-327	Cl	$C(CH_3)_3$	$C(CH_3)_3$
UV-328	–	$C(CH_3)_2CH_2CH_3$	$C(CH_3)_2CH_2CH_3$
UV-329	–	$C(CH_3)_2CH_2C(CH_3)_3$	–

The main purpose of this study was to decipher the underlying molecular mechanisms by investigating how BZTs with different structural moieties affect HSA at the atomic level. By using our novel HSA biosensor and multiple spectroscopies, we probed the interactions of HSA upon the binding of six BZTs, i.e., UV-326, UV-327, UV-328, UV-329, UV-P and BZT (Table 1). The versatile molecular dynamics (MD) simulations were further performed to provide atomic insight into the different molecular recognitions between BZTs and HSA. The visualized binding details were also exhibited by molecular modeling method and the results could agree well with that from the experimental study (Lv et al., 2013). To the best of our knowledge, this is the first *in vitro* and *in silico* study on the characterization of interactions between BZTs and HSA. Our results will be beneficial to understanding the structure-activity relationships (SAR) of BZTs and provide essential data toward future design of environmental benign BZTs-related materials.

2. Materials and methods

2.1. Reagents and chemicals

BZTs (Table 1) with purity above 96% were purchased from TCI (Tokyo, Japan). HSA was purchased from Sigma Sloaribio (Beijing, China). Flufenamic acid and oleic acid used to probe binding site were purchased from Sigma Aldrich (St. Louis, MO, USA). All other chemicals and reagents were of analytical grade. Tris–HCl buffer (0.2 M Tris, 0.1 M NaCl, pH 7.4) was used as a stock solution for fluorescence spectra experiments. Phosphate buffer (0.02 M, pH 7.4) was used for circular dichroism (CD) measurements to minimize the interference of chloride ions. All aqueous solutions were prepared with distilled water (18.2 MΩ, Millipore, Bedford, MA).

2.2. Measurement of electrochemical impedance by HSA biosensor

The HSA biosensor was designed following a recently reported

protocol (Lu et al., 2014). Bearing the advantage of the high electrode coverage and the uniform electric field, the interdigitated golden electrodes were applied to monitor the electrochemical impedance changes upon the binding of BZTs to HSA. Prior to the detection, an electrode chip with two groups of eight channels was fabricated (Liu et al., 2010). The solution of nitrocellulose membrane (Shanghai Haoran Biological Technology Co., China) and methanol were prepared with the ratio of membrane area (mm^2) to methanol volume (μl) close to 1:3. After the evaporation of methanol, 15 μl solution was added on the interdigitated golden electrodes for the immobilization followed by the injection of 50 μl HSA solution at 132 μg/ml on the nitrocellulose membrane. HSA was incubated at 22 °C for 2 h to allow the total embedment of HSA in the nitrocellulose membrane. The unbound HSA was then rinsed off with PBS buffer. The Zahner ZENNIUM electrochemical workstation (Zahner Elektrik, Germany) was used for the impedance measurements under the frequency range of 1 Hz–100 kHz and a 5 mV alternating voltage. BZTs at different concentrations were added to the same plate well containing 5 mM $K_4[Fe(CN)_6]/K_3[Fe(CN)_6]$ (1:1, v/v). The electrochemical impedance spectroscopy was recorded for 40 min at 22 °C.

2.3. CD spectroscopy

Jasco J-815 CD spectropolarimeter (JASCO Corporation, Japan) was used to monitor the far-UV CD spectra of HSA (2 μM) in the absence of BZTs (apo HSA) or in the presence of 0–6 μM BZTs (bound HSA) with a 1-cm quartz cell. The CD spectra were recorded at 298 K in triplicate from 200 to 260 nm at a scanning speed of 50 nm/min. To avoid possible solvent interference, all the spectra were corrected with the appropriate blanks.

2.4. Fluorescence spectroscopy

Fluomax®-4 spectrofluorimeter (Horiba Jobin Yvon IBH) was used for all fluorescence spectra measurements. Apo HSA and bound HSA solutions were placed in a 1-cm quartz cuvette. For the steady-state fluorescence quenching, the excitation wavelength was set at 295 nm and the emission wavelength ranged from 300 to 450 nm. The fluorescence emission spectra at 298 K and 310 K were recorded with an integration time of 0.2 s. The entrance and exit slits were both set at 5 nm. The inner filter effect was eliminated during the fluorescence spectra analysis.

The time-resolved fluorescence of apo HSA and bound HSA was measured by the time-correlated single-photon counting (TCSPC) method following the reported protocol (Zhang et al., 2013a, b). The picosecond diode laser NanoLED-280 (pulse width <1 ns) was chosen as the excitation source and the emission was monitored at 358 nm. For both excitation and emission, a 5-nm slit was used. DAS 6.6 decay analysis software (HORIBA Jobin-Yvon) was used to analyze lifetime components and the goodness of fit was evaluated by chi-square values (0.9–1.2).

2.5. Molecular docking

Because of the unavailable X-ray crystal structures or NMR structures of BZTs-HSA complexes, the tertiary structures of HSA-BZT complexes were constructed by molecular docking with a reported protocol (Zhuang et al., 2014, 2012). The crystal structure of HSA (PDB entry: 2BXF, 2.95 Å [10]) was used as the initial template. The conformations were searched for thirty times using the automatic genetic algorithm (GA) for each docking. Thirty conformational poses were finally obtained and their binding energies were scored by GoldScore algorithm and rescored by ChemPLP algorithm. Diazepam was successfully pre-docked into HSA by Gold 5.0 program (Cambridge Crystallographic Data Center) to validate the docking protocol and the obtained pose of diazepam has a RMSD of 0.41 Å. Six BZTs were finally docked into the binding site of HSA and the obtained poses were further used for MD simulations.

2.6. MD simulations

To further explore the conformational space of HSA upon the binding of BZTs, MD simulations were performed on BZTs-HSA complexes using Amber 12 package following the reported protocols (Ding et al., 2015; Zhuang et al., 2014). Based on the tertiary structures constructed from molecular docking, the topology and coordinated files for MD simulations were prepared by Amber tools 1.5 using AMBER03 force field (Duan et al., 2003) and GAFF force field. The RESP (restrained electrostatic potentials) atomic partial charges of BZTs were derived via R.E.D. Server (Vanquelef et al., 2011). BZTs-HSA complexes were solvated in a rectangular parallelepiped box with 10 Å TIP3P explicit waters and subsequently neutralized with 14 Na^+ ions. The final systems have a total of approximately 81,000 atoms (Table S1). The prepared MD systems were then minimized, heated to 300 K and finally simulated for 10 ns in an isothermal-isobaric (NPT) ensemble with a time step of 2 ps. The nanosecond MD simulations are usually considered reliable to investigate local conformational changes (Yeggoni et al., 2014). Based on the obtained 10 ns MD trajectories, 200 conformations sampled with an interval of 50 ps were used to evaluate the binding free energies of BZTs to HSA by molecular mechanics generalized Born/surface area (MMGB/SA) method.

3. Results and discussion

3.1. Conformational changes induced by BZTs

The potential conformational changes of HSA upon the binding of BZTs were characterized by an array of electrochemical and spectroscopic methods, including a HSA biosensor designed for monitoring the induced electrochemical impedance changes upon the binding of BZTs, CD spectroscopy for the measurement of α-helix content and the band intensity, fluorescence spectroscopy for measuring spectra quenching and fluorescence lifetime decay, and MD simulations for monitoring conformational changes of HSA at the atomic level.

Firstly, we successfully designed a HSA biosensor for the sensing of impedance process during the interactions of BZTs with HSA. A Randles cell circuit (Fig. 1, inset) was constructed to simplify the impedance sensing process, which was previously applied to detect electrochemical molecular recognition of floral odors and pheromones (Lu et al., 2014). This circuit was constituted by the solution resistance (R_s), the constant phase element (CPE), the Warburg impedance (Z_w) and the charge transfer resistance (R_{ct}). R_{ct} was chosen as the sensing parameter for monitoring the BZT-HSA interactions. The recorded Nyquist plots (Im (Z) vs. Re (Z)) obtained from the electrochemical experiment demonstrated the impedance spectra of BZTs (Fig. 1). The diameter of the semicircle of the Nyquist plot equals R_{ct}, whereas the changes in R_{ct} reflect the binding of BZTs to the immobilized HSA, which leads to a decreased efficiency of the electron transfer. BZTs bear heterocyclic benzazole moiety and the electron withdrawing imine (–C=N–) leads to their high electron transporting ability. The binding of BZTs to HSA causes the changes of the dielectric or conductive properties of HSA on the electrodes, indicative of conformational changes of HSA. The R_{ct} values become larger with the increasing concentration of BZTs, illustrating concentration-dependent impedance spectra. Although the impedance spectra of UV-327, UV-329, and BZT bear similar characteristics, the impedance increase of BZT was larger than that

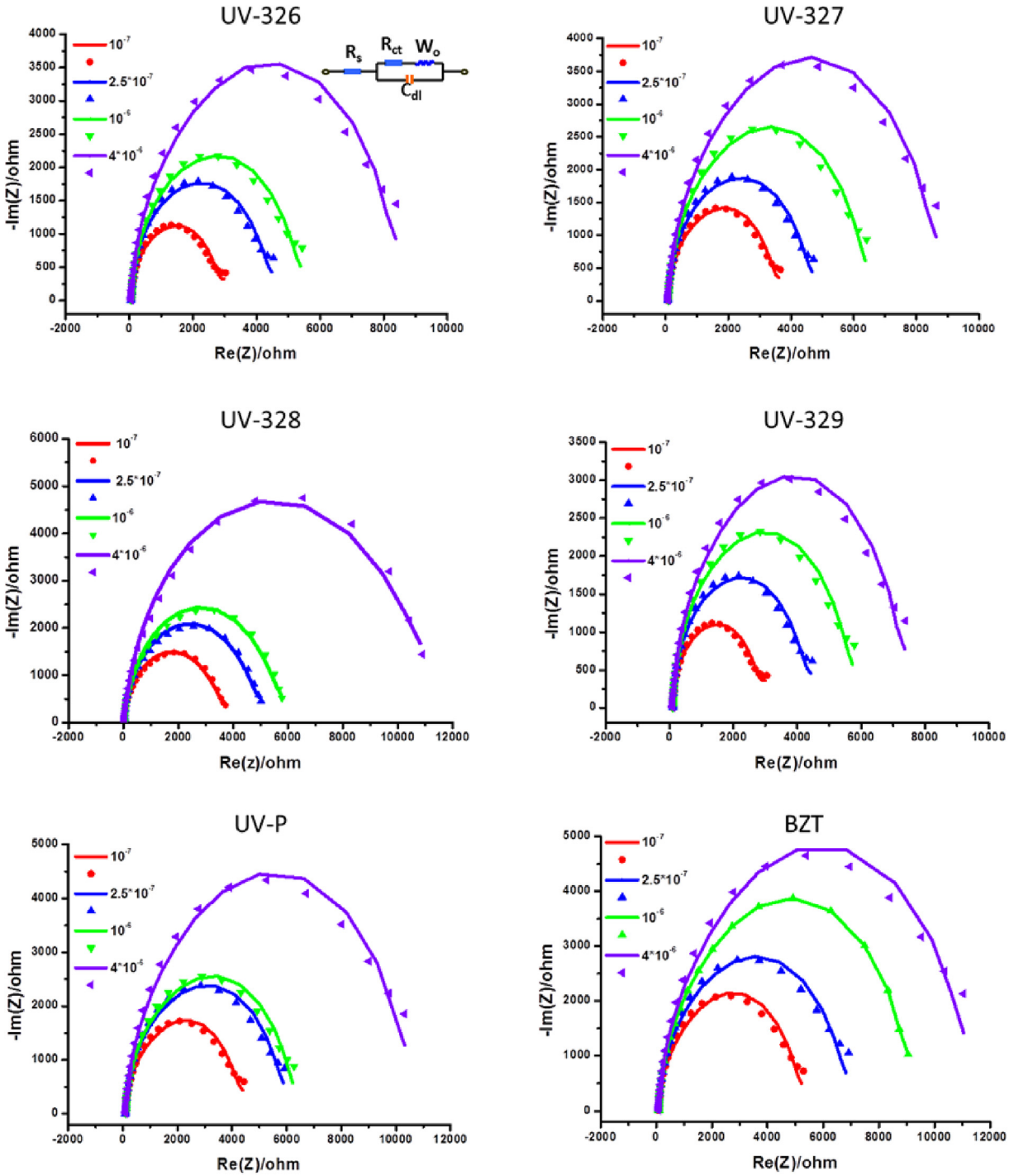

Fig. 1. The Nyquist plots of impedance spectra of HSA complexed with six BZTs at1×10^{-7} M, 2.5×10^{-7} M, 1×10^{-6} M, and 4×10^{-6} M. The symbols are the experimental data and the lines represent the simulated spectra. A Randles cell shown in the inset is an equivalent electrical circuit that consists of four elements: the solution resistance (R_s), the constant phase element (CPE), the Warburg impedance (Z_w), and the charge transfer resistance (R_{ct}).

of UV-327 and UV-329, suggesting that the designed HSA biosensor is highly specific to individual BZTs.

Secondly, our CD experiments revealed the global structural changes of HSA upon the binding of BZTs. As shown in Fig. 2, apo HSA exhibits two negative bands at 208 and 222 nm corresponding to the α-helix structure. The binding of six BZTs decreased the intensity of CD signals of HSA at 208 and 222 nm and the reduced CD signals became more pronounced with increasing BZTs concentrations, indicating the concentration-dependent disruption of the secondary structure of HSA. The apo HSA has a high α-helix content of 51.9%, in line with the reported values of 51.6%–51.9% (Chi and Liu, 2011; Zhang et al., 2013a, b; Pan et al., 2011). After titrating BZTs to HSA with a molecular ratio of 1:1, the α-helix content of HSA reduced by 48.6%, 46.6%, 49.7%, 48.0%, 50.3%, and 48.3% for UV-326, UV-327, UV-328, UV-329, UV-P and BZT, respectively, indicating the partial disruption of the secondary structure of HSA upon the binding of BZTs. The varying degree of reduced α-helix content indicates different binding effects of BZTs on critical HSA residues

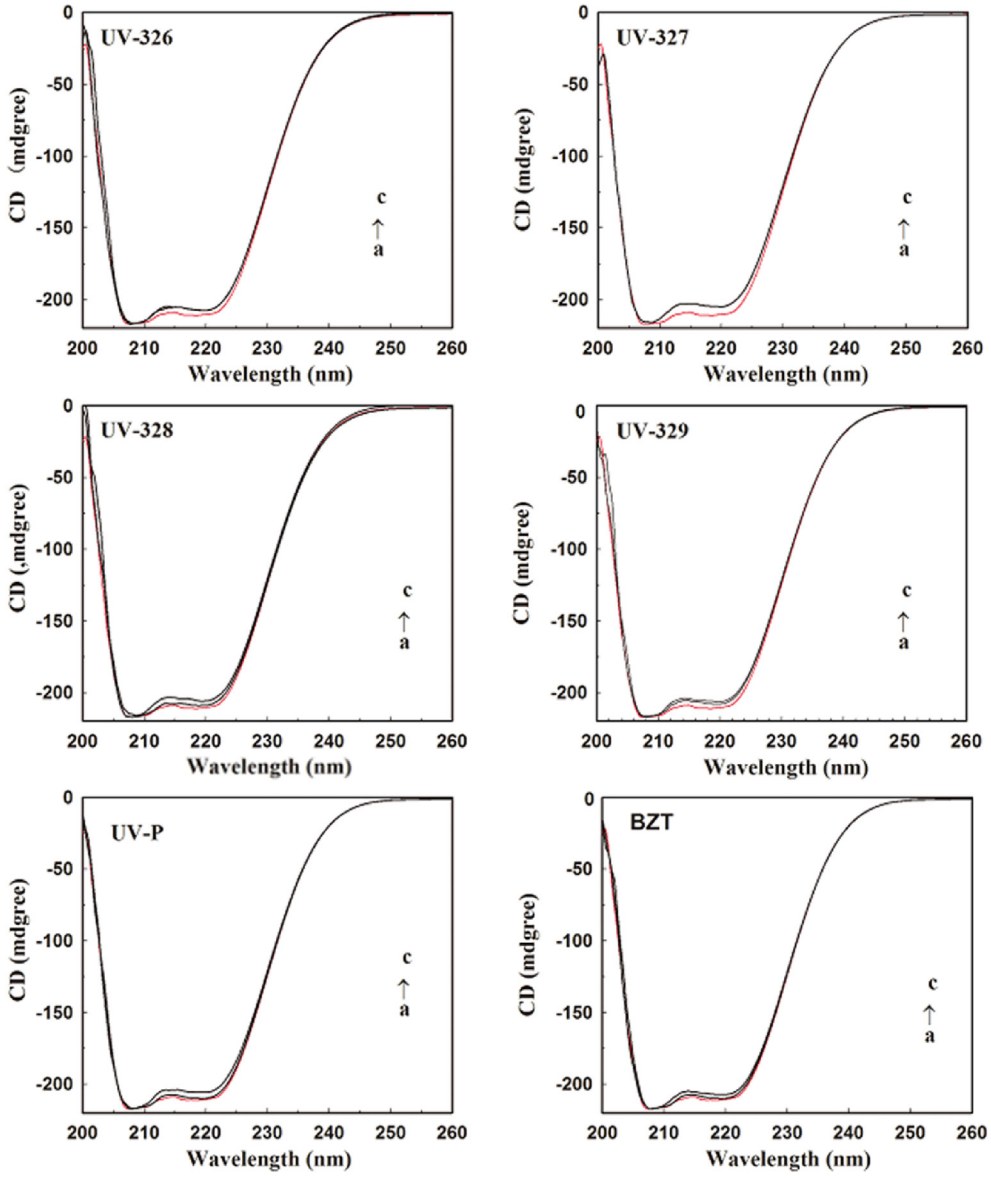

Fig. 2. Circular dichroism (CD) spectra of apo HSA (in red) and HSA bound with six BZTs (in black). Conditions: [HSA] = 2×10^{-6} mol/L; a to c stands for the concentration of BZTs at 0 mol/L, 2×10^{-6} mol/L and 6×10^{-6} mol/L, respectively; pH = 7.40. (For interpretation of the references to color in this figure legend, the reader is referred to the web version of this article.)

potentially involved in their interactions. The decreased percentage of α-helical structure indicated that BZTs bound to the amino acid residues of the backbone chain of HSA and destroyed the hydrogen bonding networks, further causing partial unfolding of protein. UV filters located in site II (sub-domain IIIA) of bovine serum albumin (BSA) were recently reported to disrupt the α-helical stability of BSA mainly through hydrogen bonding and hydrophobic interaction (Ao et al., 2015).

Complementary to CD measurements, the 3D fluorescence spectra were measured for HSA. The intrinsic fluorescence spectroscopy can sensitively detect biomolecule receptors and their interactions with various ligands. Fig. 3 shows three emission-excitation matrices of HSA in the absence and presence of BZTs, which consists of two main peaks. The intensity of two peaks is correlated with the secondary structure of HSA. Peak A exhibits the combined fluorescence spectral behavior of residues Trp and Tyr, while peak B is generally regarded as the fluorescence signatures of the polypeptide scaffold. For peak A and peak B, the ratio of fluorescence intensity before and after the titration of UV-326, UV-327, UV-328, UV-329 UV-P and BZT are 1.27 vs. 1.21, 1.36 vs. 1.83, 1.19 vs. 1.13, 1.19 vs. 1.47, 1.27 vs. 1.73, 1.73 vs. 2.05, respectively. Compared with that of apo HSA, the band intensities of two peaks decreased after the titration of BZTs, indicating the changed polypeptide structures of HSA upon the binding of BZTs. This validates the observation of CD spectra.

For dynamic quenching, when the temperature of the system rises, the effective collision times between molecules, the energy transfer efficiency, and the fluorescence quenching constants of substances all increase. For static quenching, increased temperature reduces the stability of the complex formed, resulting in a reduced quenching constant (Zhao et al., 2009). Our *in vitro* steady-state fluorescence quenching measurement showed that the emission spectrum of apo HSA exhibits a single peak maximum at 358 nm (Fig. S1). If the small molecule can quench the tryptophan residues, the residues should be located at or near the binding position (Zhao et al., 2011). After the titration of BZTs to HSA

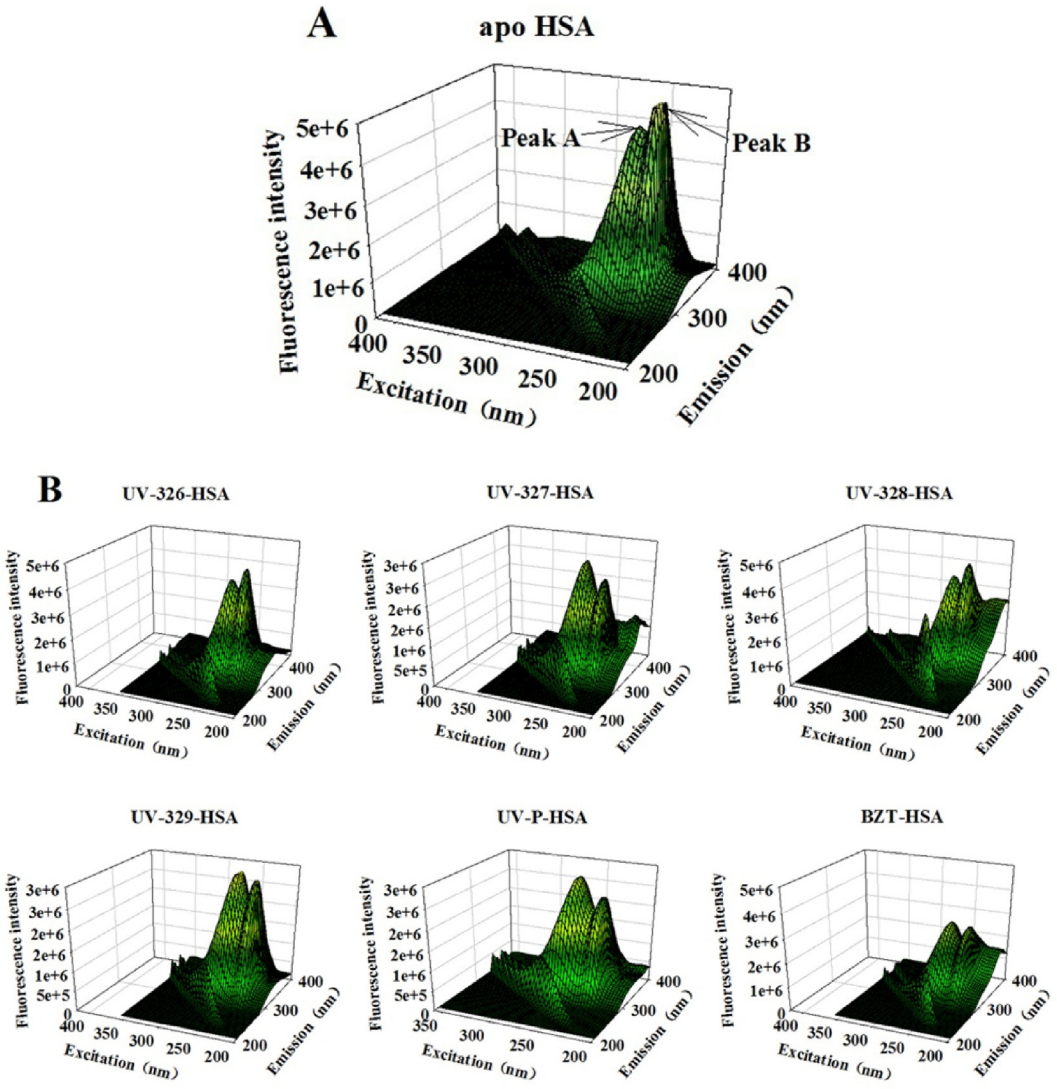

Fig. 3. The 3D fluorescence spectrum of HSA in the absence (a) and presence (b) of six BZTs. Peak A and peak B stands for the fluorescence signatures of residues Trp and Tyr, polypeptide scaffold, respectively.

solution, the fluorescence intensity at λ_{em} = 358 nm decreased markedly with the increasing concentration of BZTs from 1 μM to 5 μM, illustrating a concentration-dependent static quenching of HSA fluorescence. Among six BZTs, UV-329 and UV-P showed more reduced fluorescence intensities of HSA. The single emission peak maximum at 358 nm indicates that Trp214 is partially buried (Abou-Zied and Al-Shihi, 2008). This peak maximum shifts slightly toward a longer wavelength from 358 nm to 362 nm, 360 nm, 360 nm, 359 nm, 360 nm, and 359 nm after the titration of UV-326, UV-327, UV-328, UV-329, BZT, and UV-P, respectively. This slight red-shift of HSA emission highly indicates conformational changes of HSA in association with the alteration of hydrophobic microenvironment around Trp214.

To confirm the steady-state fluorescence observations, we further measured the fluorescence decay of HSA in the absence and presence of BZTs (Table 2). The lifetimes of HSA consist of two main components, one shorter decay (τ_1) and one longer decay (τ_2). The reported lifetime of τ_1 is around 1.0–3.5 ns and that of τ_2 between 5.5 and 8.0 ns (Åqvist et al., 2002). Our biexponential curve fitting for the fluorescence decay of apo HSA resulted in two lifetime components (1.82 and 4.46 ns, Table 2), in line with the reported fluorescence decay. The total lifetime of HSA (τ) remains unchanged during the titration of BZTs (Fig. S2). However, compared with apo HSA, τ_1 and τ_2 of HSA in the presence of BZTs were affected in a greater extent, especially the τ_1 value for UV-329/HSA and UV-P/HSA complex. Since the fluorescence decay is predominantly contributed by Trp214 of HSA, the change of fluorescence lifetime

Table 2
Time-resolved fluorescence decay of HSA[a].

System	τ_1 (ns)	τ_2 (ns)	A_1	A_2	τ (ns)[b]
apo HSA	1.82	4.46	0.14	0.86	4.04
UV-326/HSA	1.71	4.52	0.15	0.85	4.04
UV-327/HSA	1.71	4.37	0.13	0.87	4.00
UV-328/HSA	1.83	4.42	0.15	0.85	4.02
UV-329/HSA	1.19	4.33	0.10	0.90	4.04
UV-P/HSA	1.44	4.32	0.11	0.89	4.05
BZT/HSA	1.79	4.25	0.10	0.90	4.03

[a] 2 μM HSA and 1 μM BZTs were used for the measurement of time-resolved fluorescence decay.

[b] The total lifetime (τ) consists of two components, the shorter decay (τ_1) and the longer decay (τ_2). A_1 and A_2 are the corresponding fractional contribution for τ_1 and τ_2, respectively.

components indicates the disruption of microenvironment surrounding Trp214. The shorter lifetimes of these two complexes indicate a stronger quenching effect on HSA, in agreement with the steady-state fluorescence quenching observed for UV-329 and UV-P.

As a versatile tool lastly, MD simulations were used to monitor the conformational changes over the time span of ligands binding (Salvalaglio et al., 2010). MD simulations for over 10 ns were performed on the tertiary structures of BZT-HSA complexes (Table S1). Such MD simulations at a nanosecond timescale are frequently used for studies on local conformations of HSA (Yeggoni et al., 2014; Beesoon and Martin, 2015; Han et al., 2013). For example, MD simulations of HSA in complex with perfluorooctanoic acid (PFOA) and perfluorooctane sulfonate (PFOS) were performed for 10 ns (Salvalaglio et al., 2010; Beesoon and Martin, 2015), HSA complexed with PCB 153 for 5 ns (Han et al., 2013), and more recent simulations of HSA with dipeptide ligand and fatty acids for 20 ns and 50 ns, respectively (Aghaee et al., 2014; Ahalawat and Murarka, 2015). The conformational space of HSA in complex with BZTs was thoroughly sampled and BZTs-induced conformational changes of HSA are depicted in Fig. S3. With the minimized tertiary structure of HSA as the reference, the RMSD of Cα atom was measured for the conformational changes of apo HSA and BZT-bound HSA along 10 ns trajectories. The averaged RMSD of apo HSA is 3.69 Å. Following the binding with UV-326, UV-327, UV-328, UV-329, BZT and UV-P, the averaged RMSD reduced to 3.29 Å, 2.29 Å, 2.99 Å, 2.44 Å, 3.33 Å and 3.32 Å. The reduced averaged Cα RMSD further indicates BZT-induced conformational changes of HSA. Compared with apo HSA (black dashed line in Fig. S3), conformational changes were observed to be slight for UV-P, BZT and UV-326, moderate for UV-328, and significant for UV-327 and UV-329. This *in silico* structural observation is generally in line with the CD assay that the α-helix content of HSA was reduced the most by UV-327 and UV-329, followed by UV-328 and UV-P with the exception of UV-326 and BZT. The superimposition of snapshot of apo HSA with that of BZTs-bound HSA (Fig. S4) at 10 ns revealed changes of the whole conformation of BZT-bound HSA, especially changes of the C terminal III B domain.

3.2. Binding characteristics of BZTs to HSA

To further decipher the mechanism of the observed quenching, the fluorescence quenching of HSA at 298 K and 310 K was analyzed by the following Stern-Volmer quenching equation:

$$\frac{F_0}{F} = 1 + K_{SV}[Q] = 1 + K_q\tau_0[Q] \quad (1)$$

where *Fo* and *F* stand for the fluorescence intensity in the absence and presence of a quencher; *Ksv* is Stern-Volmer constant (L/mol) estimated by curve fitting of the Stern-Volmer quenching equation; [*Q*] is the concentration of BZTs (mol/L); τ_0 is the total lifetime (4.04 ns) determined from our fluorescence decay (Table 2); *Kq* is the quenching rate constant of HSA calculated by Ksv/τ. The calculated *Kq* values of 10^{11}–10^{12} L/(mol ·s) (Table S2) have one order of magnitude higher than the maximum dynamic collisional quenching constant [2.0×10^{10} L/(mol ·s)] of biomacromolecules, suggesting a static quenching mode for BZT-HSA complexes. To further confirm the static fluorescence quenching, the steady-state fluorescence quenching assay was performed at 310 K. K_{sv} values decreased with an elevated temperature (Table S2, Fig. S5), thereby confirming the static quenching mechanism (Ross and Rekharsky, 1996). The total fluorescence lifetime of HSA remains unchanged during the titration of BZTs (i.e., independent of BZT concentrations) (Table 2, Fig. S2), further confirming the static quenching occurred during the formation of BZT-HSA complex.

HSA generally has two main ligand binding sites, Sudlow site I and Sudlow site II. The binding equilibrium between apo HSA and BZT-bound HSA is described by the following Scatchard equation:

$$\log\left(\frac{F_0 - F}{F}\right) = \log K_A + n\log[Q] \quad (2)$$

where K_A represents the binding constant (L/mol); *n* is the number of binding sites; K_A and *n* were calculated from the linear plot between F_0/F and [*Q*] (Fig. S5). The obtained values of *n* are close to 1 (Table S3), indicating that all six BZTs are located at only one binding site of HSA. We further determined the binding site of BZTs by the competitive binding fluorescence assay using oleic acid (probe of Sudlow site I) and flufenamic acid (probe of Sudlow site II) as the probe. As shown in Table S4 and Fig. S6, the K_a of BZTs decreased significantly upon the titration of oleic acid, while it changes little changed in the presence of flufenamic acid, indicating that BZTs bind only at Sudlow site I.

3.3. Binding mode and binding energies analysis

The general lack of the X-ray crystal structures or NMR structures of HSA in complex with various ligands impedes the investigation of their molecular interactions. Our MD simulations revealed that six BZTs were orientated differently at Sudlow site I of HSA and they were surrounded mainly by residues Trp214, Arg218, Arg222, His242, Arg257, and Glu292 (Fig. 4). These residues are the key determinants of binding specificity for BZTs (Ghuman et al., 2005). The binding of BZTs partially disturbs the hydrophobicity of Sudlow site I and the penetration of molecules into Sudlow site I. UV-327 forms one hydrogen bond with residue Arg257, whereas UV-329 forms one hydrogen bond with Leu238 and two hydrogen bonds with two water molecules. The ring of Trp214 is headed toward one end of BZTs molecule, while the ring of Trp214 is parallel to the ring of BZT, forming π-π interactions. The binding of BZTs significantly shifts the orientation of Trp214 toward Arg218 and His242, which at least partially explains why BZTs induce the concentration-dependent impedance spectra, decrease the α-helix content and change the lifetime components of HSA. Previous studies on time-resolved fluorescence anisotropy demonstrated that the indole functional group of Trp exhibits much freedom of rotation at the timescale of subnanosecond (Ross et al., 1981). This is consistent with the observation from our MD simulations that Trp214 can be re-oriented upon the binding of BZTs. Trp214 was also involved in the hydrophobic packing interaction of the IIA-IIIA interface. The re-orientation of Trp214 of Sudlow site I may induce conformational changes in Sudlow site II as well (Gokara et al., 2010; Sahoo et al., 2009) and thus further alters the conformation of HSA, confirming a slight but definitive partial unfolding on complexation (Khan et al., 2012).

The thermodynamic parameters such as binding free energy change (ΔG), enthalpy change (ΔH), and entropy change (ΔS) were also evaluated. As shown in Table 3, values of ΔH and ΔG for six BZTs-HSA complexes are all negative, suggesting that BZTs bind to HSA via spontaneous processes (Chen et al., 2015). UV-P, UV-329 and BZT have the positive ΔS, while UV-326, UV-327 and UV-328 have the negative ΔS. The negative ΔH together with positive ΔS suggests that the electrostatic interactions and hydrophobic interactions play a significant role in the interactions of UV-P, UV-329 and BZT with HSA. The negative ΔH coupled with negative ΔS for UV-326, UV-327 and UV-328 indicates that van der Waals force or hydrogen-bonding contributes mostly to their interactions with HSA. The measured binding constants at 298 K range from 0.32×10^4 L/mol to 2.96×10^4 L/mol (Table 3). In comparison with

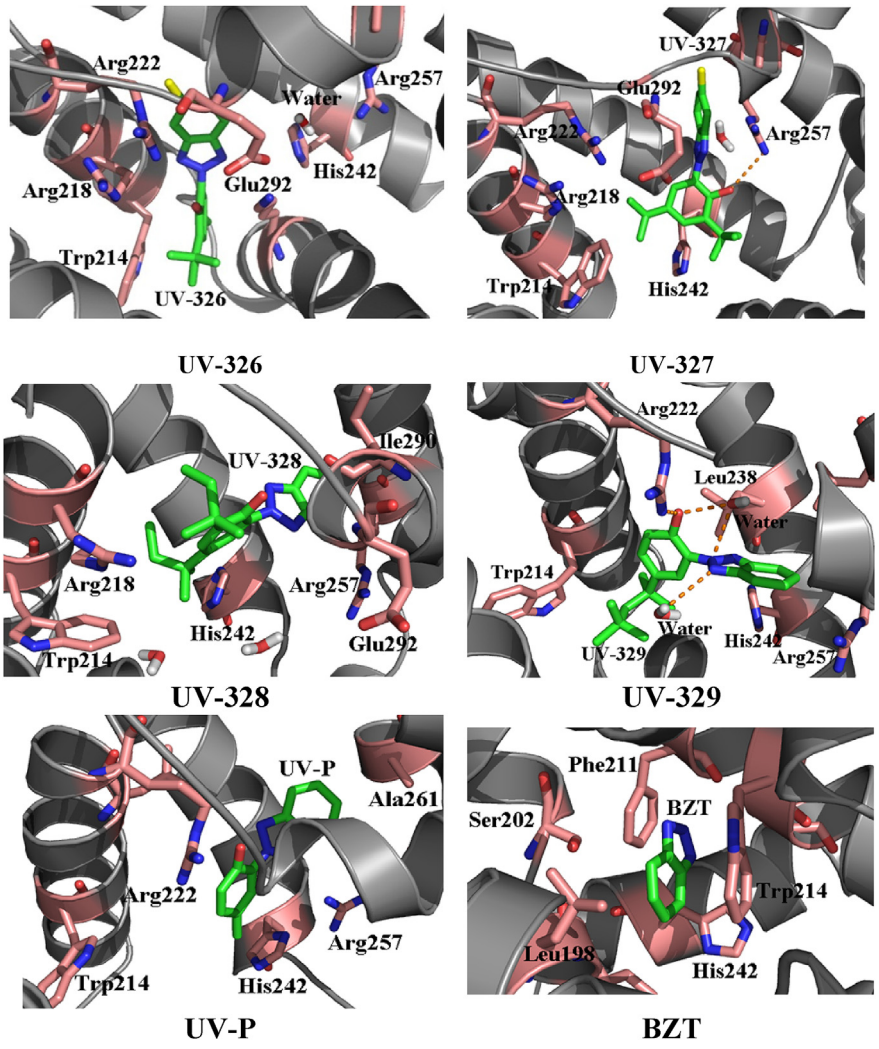

Fig. 4. The binding mode of BZTs to HSA. BZTs and surrounding residues were represented in the sticks form. HSA was shown as the cartoon form. BZTs, key residues, and HSA were colored in green, pink and grey, respectively. (For interpretation of the references to color in this figure legend, the reader is referred to the web version of this article.)

ketoprofen and polyamine analogues bound to HSA with a binding constant of 10^2–10^4 L/mol at 298 K, BZTs have a relatively stronger binding potency (Bi et al., 2011).

The binding free energies of six BZTs were further decomposed using MMGB/SA methods (Table S5). A simulation time of 10 ns is generally sufficient to evaluate binding affinities by MM-PB/GBSA methods (Xu et al., 2013). The total binding free energies (ΔG_{calc}) in Table S5 are the sum of van der Waals interaction (ΔE_{vdw}), electrostatic interactions (ΔE_{ele}) and gas-phase solvation energy (ΔE_{sol}). The decomposition of the binding free energies showed that van der Waals, electrostatic and hydrophobic interactions (ΔE_{surf}) are favorable for the interactions of BZTs with HSA. The chlorine

Table 3
The measured association constants (K_a) and thermodynamic parameters.

Compound	Temperature (K)	K_a ($\times 10^4$ L/mol)	r^a	ΔH (kJ/mol)	ΔS (J/mol)	ΔG (kJ/mol)
UV-326	298	2.21	0.999	−85.62	−204.15	−24.78
	310	0.58	0.998			−22.33
UV-327	298	1.96	0.999	−101.72	−259.16	−24.49
	310	0.40	0.998			−21.38
UV-328	298	1.60	0.998	−97.28	−245.94	−23.98
	310	0.35	0.997			−21.03
UV-329	298	2.96	0.997	−16.72	29.54	−25.51
	310	2.28	0.999			−25.86
UV-P	298	2.28	0.997	−3.46	71.81	−24.86
	310	2.16	0.998			−25.72
BZT	298	0.32	0.997	−8.55	38.42	−20.00
	310	0.28	0.996			−20.46

r^a = correlation coefficient for the K_a values.

atom and alkyl groups of different sizes contained in R1, R2 and R3 moieties (Table 1) contribute differently to the van der Waals and hydrophobic interactions. UV326, UV-327, UV-328 and UV-329 have much higher van der Waals and hydrophobic interactions than that of UV-P and BZT (Table S5). As reported previously, the halogen bonds and hydrophobic interactions of tetrabromobenzotriazole and some C5-substituted analogues are of significance to their inhibition of human protein kinase CK2α (Wasik et al., 2010). As characterized by LogP (a well-established measure of lipophilicity), the chlorine atom and alkyl groups improve the molecular hydrophobicity of BZTs. Due to the chlorine atom and alkyl groups in R1, R2 and R3 moieties, there exists a high correlation of LogP with ΔE_{surf} ($R^2 = 0.8946$) and ΔE_{vdw} ($R^2 = 0.8513$) (Fig. S7). The halogenation in 3, 5-positions of the phenolic rings of bisphenol A was reported to result in more van der Waals contacts (Zhuang et al., 2014). The chlorine atom in R1 position of UV-326 and UV-327 increased the molecular hydrophobicity (Table S6). The absolute value of ΔE_{vdw} for UV-326 and UV-327 is much higher than that of other BZTs, in line with the fluorescence observation of UV-326, UV-327 and UV-328 that their negative ΔH coupled with negative ΔS indicates the main contribution of van der Waals forces or hydrogen-bonding to the interactions with HSA. The larger alkyl group of R2 moiety for U-327 causes higher molecular hydrophobicity, ΔE_{surf} and ΔE_{vdw} in comparison with UV-326. UV-328 and UV-329 also have high van der Waals and hydrophobic interactions due to their larger alkyl moiety in R2 or R3 position.

The electron-withdrawing chlorine atom and electron-donating alkyl groups can potentially affect the molecular electrostatic potentials (ESP) distribution of phenolic ring and benzotriazole ring. To characterize the different electrostatic interactions, ESP distribution of six BZTs were calculated with Gaussian 09 program using density functional theory (DFT) at the B3LYP/6−311++G (d, p) level. The positive and negative ESP (Fig. S8, blue and red, respectively) illustrates quite different distribution of ESP over the entire molecule of BZTs, contributing differently to the electrostatic interactions with HSA (Table S5). The electrostatic interaction was recently reported to be critical to distinct interactions of bisphenol A analogues with peroxisome proliferator-activated receptor (PPAR) γ and estrogen receptor (ER) α receptors (Zhuang et al., 2014). UV-P, BZT and UV-329 have more negative ΔE_{ele} values, indicating more favorable electrostatic interactions with HSA. As revealed by the fluorescence decay and the binding mode analysis, the binding of UV-329, UV-P and BZT induced re-orientation of Trp214 and disturbed surrounding microenvironment (Fig. 4), resulting in more favorable electrostatic interactions.

4. Conclusions

This study provided an atomic insight into the molecular recognition of six BZTs toward HSA by the integrated approaches of our novel HSA biosensor, CD spectroscopy, fluorescence spectroscopy and MD simulations. Both *in vitro* and *in silico* studies revealed how various BZTs affect HSA differently. Our study showed that all BZTs bind to HSA tightly at Sudlow site I of HSA, but induce different concentration-dependent conformational changes of HSA owing to the specific molecular recognition, primarily caused the re-orientation of Trp214. The perturbed microenvironment of Sudlow site I and the impaired secondary structures of HSA by BZTs may cause potential structural damages of HSA and thus may lead to the disturbance of normal biological functions of HSA. The electrostatic interactions were revealed as the critical contributor to the various interactions between BZTs and HSA. Our structure-activity relationships (SAR) study revealed that minor changes in the moieties of BZTs may affect their interactions with HSA and also induce differently conformations of HSA. The future design of BZTs should fully examine the structural moieties that could lead to the desired properties as well as those unwanted environmental and public health outcomes. It is prudent to conclude that our approaches not only provide beneficial information to the risk assessment of BZTs-containing materials, but also offer a framework for the study of ligands binding with biomacromolecules. This study raises critical concerns regarding the transportation, distribution and toxicity effects of organic UV filters in human body.

Competing interests

The authors declare no competing financial interest.

Acknowledgments

This project was sponsored by the National Natural Science Foundation of China (No. 21477113, 21277122, 81371643), the Major Science and Technology Projects of Zhejiang Province (No. 2014C03026), the Cultivation Fund of the Key Scientific and Technical Innovation Project, Ministry of Education of China (No. 708052) and the Fundamental Research Funds for the Central Universities. CZ gratefully acknowledged Welch Foundation for partial support.

Appendix A. Supplementary data

Supplementary data related to this article can be found at http://dx.doi.org/10.1016/j.chemosphere.2015.09.085.

References

Abou-Zied, O.K., Al-Shihi, O.I., 2008. Characterization of subdomain IIA binding site of human serum albumin in its native, unfolded, and refolded states using small molecular probes. J. Am. Chem. Soc. 130, 10793–10801.
Aghaee, E., Ghasemi, J., Manouchehri, F., Balalaie, S., 2014. Combined docking, molecular dynamics simulations and spectroscopic studies for the rational design of a dipeptide ligand for affinity chromatography separation of human serum albumin. J. Mol. Model 20, 2446–2446.
Ahalawat, N., Murarka, R.K., 2015. Conformational changes and allosteric communications in human serum albumin due to ligand binding. J. Biomol. Struct. Dyn. 33, 2192–2204.
Ao, J., Gao, L., Yuan, T., Jiang, G., 2015. Interaction mechanisms between organic UV filters and bovine serum albumin as determined by comprehensive spectroscopy exploration and molecular docking. Chemosphere 119, 590–600.
Åqvist, J., Luzhkov, V.B., Brandsdal, B.O., 2002. Ligand binding affinities from MD simulations. Accounts. Chem. Res. 35, 358–365.
Beauchemin, R., N'Soukpoe-Kossi, C.N., Thomas, T.J., Thomas, T., Carpentier, R., Tajmir-Riahi, H.A., 2007. Polyamine analogues bind human serum albumin. Biomacromolecules 8, 3177–3183.
Beesoon, S., Martin, J.W., 2015. Isomer-specific binding affinity of Perfluorooctanesulfonate (PFOS) and Perfluorooctanoate (PFOA) to serum proteins. Environ. Sci. Technol. 49, 5722–5731.
Bi, S., Yan, L., Sun, Y., Zhang, H., 2011. Investigation of ketoprofen binding to human serum albumin by spectral methods. Spectrochim. Acta. A. 78, 410–414.
Bischel, H.N., Macmanus-Spencer, L.A., Luthy, R.G., 2010. Noncovalent interactions of long-chain perfluoroalkyl acids with serum albumin. Environ. Sci. Technol. 44, 5263–5269.
Chen, H., He, P., Rao, H., Wang, F., Liu, H., Yao, J., 2015. Systematic investigation of the toxic mechanism of PFOA and PFOS on bovine serum albumin by spectroscopic and molecular modeling. Chemosphere 129, 217–224.
Chi, Z., Liu, R., 2011. Phenotypic characterization of the binding of tetracycline to human serum albumin. Biomacromolecules 12, 203–209.
Ding, K., Zhang, H., Wang, H., Lv, X., Pan, L., Zhang, W., Zhuang, S., 2015. Atomic-scale investigation of the interactions between tetrabromobisphenol A, tetrabromobisphenol S and bovine trypsin by spectroscopies and molecular dynamics simulations. J. Hazard. Mater 299, 486–494.
Duan, Y., Wu, C., Chowdhury, S., Lee, M.C., Xiong, G., Zhang, W., Yang, R., Cieplak, P., Luo, R., Lee, T., Caldwell, J., Wang, J., Kollman, P., 2003. A point-charge force field for molecular mechanics simulations of proteins based on condensed-phase quantum mechanical calculations. J. Comput. Chem. 24, 1999–2012.
Ghuman, J., Zunszain, P.A., Petitpas, I., Bhattacharya, A.A., Otagiri, M., Curry, S., 2005. Structural basis of the drug-binding specificity of human serum albumin. J. Mol. Biol. 353, 38–52.
Gokara, M., Sudhamalla, B., Amooru, D.G., Subramanyam, R., 2010. Molecular interaction studies of trimethoxy flavone with human serum albumin. PLoS One

5, e8834.
Han, C., Fang, S., Cao, H., Lu, Y., Ma, Y., Wei, D., Xie, X., Liu, X., Li, X., Fei, D., Zhao, C., 2013. Molecular interaction of PCB153 to human serum albumin: insights from spectroscopic and molecular modeling studies. J. Hazard. Mater 248, 313–321.
He, X.M., Carter, D.C., 1992. Atomic structure and chemistry of human serum albumin. Nature 358, 209–215.
He, T., Liang, B., Liu, W., Paul, K.S.S., Rudolf, S.S.W., 2012. Estrogenic potential of benzotriazole on marine medaka (Oryzias melastigma). Ecotox. Environ. Safe 80, 327–332.
Hirata-Koizumi, M., Matsuyama, T., Imai, T., Hirose, A., Kamata, E., Ema, M., 2008. Gender-related difference in the toxicity of ultraviolet absorber 2-(3',5'-di-tert-butyl-2'-hydroxyphenyl)-5-chlorobenzotriazole in rats. Drug. Chem. Toxicol. 31, 383–398.
Hu, Y.J., Ou-Yang, Y., Dai, C.M., Liu, Y., Xiao, X.H., 2010. Site-selective binding of human serum albumin by palmatine: spectroscopic approach. Biomacromolecules 11, 106–112.
Kandel, S.E., Lampe, J.N., 2014. Role of protein-protein interactions in cytochrome P450-mediated drug metabolism and toxicity. Chem. Res. Toxicol. 27, 1474–1486.
Khan, A.Y., Hossain, M., Suresh Kumar, G., 2012. Investigations on the interaction of the phototoxic alkaloid coralyne with serum albumins. Chemosphere 87, 775–781.
Liu, Q., Ye, W., Xiao, L., Du, L., Hu, N., Wang, P., 2010. Extracellular potentials recording in intact olfactory epithelium by microelectrode array for a bioelectronic nose. Biosens. Bioelectron 25, 2212–2217.
Lu, Y., Li, H., Zhuang, S., Zhang, D., Zhang, Q., Zhou, J., Dong, S., Liu, Q., Wang, P., 2014. Olfactory biosensor using odorant-binding proteins from honeybee: ligands of floral odors and pheromones detection by electrochemical impedance. Sens. Actuat. B. Chem. 193, 420–427.
Lv, W., Chen, Y., Li, D., Chen, X., Leszczynski, J., 2013. Methyl-triclosan binding to human serum albumin: multi-spectroscopic study and visualized molecular simulation. Chemosphere 93, 1125–1130.
Nagayoshi, H., Kakimoto, K., Takagi, S., Konishi, Y., Kajimura, K., Matsuda, T., 2015. Benzotriazole ultraviolet stabilizers show potent activities as human aryl hydrocarbon receptor ligands. Environ. Sci. Technol. 49, 578–587.
Nakata, H., Murata, S., Filatreau, J., 2009. Occurrence and concentrations of benzotriazole UV stabilizers in marine organisms and sediments from the Ariake Sea. Jpn. Environ. Sci. Technol. 43, 6920–6926.
Nakata, H., Murata, S., Filatreau, J., 2010. Detection of benzotriazole UV stabilizers in the blubber of marine mammals by gas chromatography-high resolution mass spectrometry (GC-HRMS). J. Environ. Monit. 12, 2088–2092.
Pan, X., Qin, P., Liu, R., Wang, J., 2011. Characterizing the interaction between tartrazine and two serum albumins by a hybrid spectroscopic approach. J. Agric. Food Chem. 59, 6650–6656.
Ross, J.B., Rousslang, K.W., Brand, L., 1981. Time-resolved fluorescence and anisotropy decay of the tryptophan in adrenocorticotropin-(1-24). Biochemistry 20, 4361–4369.
Ross, P.D., Rekharsky, M.V., 1996. Thermodynamics of hydrogen bond and hydrophobic interactions in cyclodextrin complexes. Biophys. J. 71, 2144–2154.
Ruan, T., Liu, R., Fu, Q., Wang, T., Wang, Y., Song, S., Wang, P., Teng, M., Jiang, G., 2012. Concentrations and composition profiles of benzotriazole UV stabilizers in municipal sewage sludge in China. Environ. Sci. Technol. 46, 2071–2079.
Sahoo, B.K., Ghosh, K.S., Dasgupta, S., 2009. Molecular interactions of isoxazolcurcumin with human serum albumin: spectroscopic and molecular modeling studies. Biopolymers 91, 108–119.
Salvalaglio, M., Muscionico, I., Cavallotti, C., 2010. Determination of energies and sites of binding of PFOA and PFOS to human serum albumin. J. Phys. Chem. B 114, 14860–14874.
Song, S., Ruan, T., Wang, T., Liu, R., Jiang, G., 2014. Occurrence and removal of benzotriazole ultraviolet stabilizers in a wastewater treatment plant in China. Environ. Sci. Proc. Impacts 16, 1076–1082.
Vanquelef, E., Simon, S., Marquant, G., Garcia, E., Klimerak, G., Delepine, J.C., Cieplak, P., Dupradeau, F.Y., 2011. R.E.D. Server: a web service for deriving RESP and ESP charges and building force field libraries for new molecules and molecular fragments. Nucleic. Acids. Res. 39, W511–W517.
Wasik, R., Lebska, M., Felczak, K., Poznanski, J., Shugar, D., 2010. Relative role of halogen bonds and hydrophobic interactions in inhibition of human protein kinase CK2α by tetrabromobenzotriazole and some C5-substituted analogues. J. Phys. Chem. B 114, 10601–10611.
Xie, X., Wang, Z., Zhou, X., Wang, X., Chen, X., 2011. Study on the interaction of phthalate esters to human serum albumin by steady-state and time-resolved fluorescence and circular dichroism spectroscopy. J. Hazard. Mater 192, 1291–1298.
Xu, L., Sun, H., Li, Y., Wang, J., Hou, T., 2013. Assessing the performance of MM/PBSA and MM/GBSA methods. 3. The impact of force fields and ligand charge models. J. Phys. Chem. B 117, 8408–8421.
Yasar, A., Matthias, J.N.J., Dariush, H., 2011. Effect of ionic liquids on the solution structure of human serum albumin. Biomacromolecules 12, 1072–1079.
Yeggoni, D.P., Gokara, M., Mark Manidhar, D., Rachamallu, A., Nakka, S., Reddy, C.S., Subramanyam, R., 2014. Binding and molecular dynamics studies of 7-hydroxycoumarin derivatives with human serum albumin and its pharmacological importance. Mol. Pharm. 11, 1117–1131.
Zhang, J., Zhuang, S., Tong, C., Liu, W., 2013a. Probing the molecular interaction of triazole fungicides with human serum albumin by multispectroscopic techniques and molecular modeling. J. Agr. Food Chem. 61, 7203–7211.
Zhang, Z., Ren, N., Li, Y.F., Kunisue, T., Gao, D., Kurunthachalam, K., 2011. Determination of benzotriazole and benzophenone UV filters in sediment and sewage sludge. Environ. Sci. Technol. 45, 3909–3916.
Zhang, F., Zhang, J., Tong, C., Chen, Y., Zhuang, S., Liu, W., 2013b. Molecular interactions of benzophenone UV filters with human serum albumin revealed by spectroscopic techniques and molecular modeling. J. Hazard. Mater 263, 618–626.
Zhao, L., Liu, R., Zhao, X., Yang, B., Gao, C., Hao, X., Wu, Y., 2009. New strategy for the evaluation of CdTe quantum dot toxicity targeted to bovine serum albumin. Sci. Total Environ. 407, 5019–5023.
Zhao, X., Liu, R., Teng, Y., Liu, X., 2011. The interaction between Ag+ and bovine serum albumin: a spectroscopic investigation. Sci. Total Environ. 409, 892–897.
Zhuang, S., Zhang, C., Liu, W., 2014. Atomic insights into distinct hormonal activities of Bisphenol A analogues toward PPARγ and ERα receptors. Chem. Res. Toxicol. 27, 1769–1779.
Zhuang, S., Zhang, J., Wen, Y., Zhang, C., Liu, W., 2012. Distinct mechanisms of endocrine disruption of DDT-related pesticides toward estrogen receptor α and estrogen-related receptor γ. Environ. Toxicol. Chem. 31, 2597–2605.